Cooperative Passivation of Perovskite Solar Cells by Alkyldimethylammonium Halide Amphiphiles

Essa A. Alharbi[1,6], Anurag Krishna[2], Nikolaos Lempesis[3], Mathias Dankl[3], Irea Mosquera Lois[3], Michael A. Hope[4], Thomas P. Baumeler[1], George Kakavelakis[1], Aditya Mishra[4], Felix Eickemeyer[1], Olivier Ouellette[1], Thanyarat Chawanpunyawat[1], Anders Hagfeldt[2], Shaik M. Zakeeruddin[1], Lyndon Emsley[4], Lukas Pfeifer[1], Ursula Rothlisberger[3*] and Michael Grätzel[1,4*]*

Affiliations:

[1] Laboratory of Photonics and Interfaces, Institute of Chemical Sciences and Engineering, Ecole Polytechnique Fédérale de Lausanne, CH-1015, Lausanne, Switzerland

[2] Laboratory of Photomolecular Science, Institute of Chemical Sciences and Engineering, École Polytechnique Fédérale de Lausanne, Lausanne 1015, Switzerland

[3] Laboratory of Computational Chemistry and Biochemistry, Institute of Chemical Sciences and Engineering, École Polytechnique Fédérale de Lausanne (EPFL), Lausanne, Switzerland

[4] Laboratory of Magnetic Resonance, Institute of Chemical Sciences and Engineering, Ecole Polytechnique Fédérale de Lausanne, CH-1015, Lausanne, Switzerland

[6] National Center for Nanotechnology and Semiconductors, King Abdulaziz City for Science and Technology (KACST), Riyadh 11442, Saudi Arabia

[*] Correspondence to Michael Grätzel (michael.graetzel@epfl.ch), Ursula Röthlisberger (ursula.rothlisberger@epfl.ch) and Lukas Pfeifer (lukas.pfeifer@epfl.ch).

Context & Scale:

Despite the rapid improvement in power conversion efficiency (PCE) of perovskite solar cells (PSCs), this technology is still facing formidable obstacles on its way towards commercialization. The main challenge is the improvement of their operational stability, an area where PSCs currently have substantial disadvantages compared to established photovoltaic technologies. This is especially true for wide-bandgap mixed halide perovskites, which suffer from halide phase segregation under illumination. Solving this issue is critical because of the importance of these materials for the development of perovskite/silicon (Si) tandem solar cells. The method presented here, based on the cooperative treatment of perovskites with a set of organic modulators, substantially improves the operational stability of PSCs including a marked suppression of halide phase segregation in mixed-halide perovskite compositions. This represents a critical step forward towards large-scale application of PSCs.

Summary:

Perovskite solar cells (PSCs) have revolutionized the field of sustainable energy research. However, their limited stability has so far impeded commercial exploitation. Here, we present two alkylammonium halide modulators that synergistically improve both power conversion efficiency (PCE) and stability of PSCs based on α-$FAPbI_3$ and $FA_{65}MA_{35}Pb(I_{65}Br_{35})_3$, while also suppressing light-induced halide phase segregation in the latter. Champion PCEs of 24.9% (α-$FAPbI_3$) and 21.2% ($FA_{65}MA_{35}Pb(I_{65}Br_{35})_3$) are reported, with ~90% and ~80% of initial PCEs retained after 1200 h and 250 h of continuous operation. 2D NMR shows the modulators are located at surfaces and grain boundaries, while their superior passivation effect compared to established compounds is rationalized using computational studies. By addressing the critical issue of stability, our results represent an important step towards large scale practical applications of PSCs.

Introduction:

Metal halide perovskites (MHPs) possess exceptional optoelectronic properties[1–4], and are, therefore, at the heart of next-generation optoelectronic devices, enabling economically viable and highly efficient photovoltaics[4,5], light-emitting diodes (LEDs)[6,7], photodetectors and lasers[3,7,8]. Over a decade of intense research on perovskite solar cells (PSCs) has allowed the power conversion efficiency (PCE) to reach certified values of 25.7% and 29.8% for single junction and perovskite/silicon (Si) tandem solar cells, respectively[9]. Most high-efficiency PSCs employ state-of-the-art α-$FAPbI_3$ as the light-absorbing layer due to its suitable bandgap (E_g) of ~1.48 eV, close to the Shockley-Queisser optimum of 1–1.4 eV[10]. However, to overcome the limitations of single-junction solar cells set by the Shockley-Queisser limit, perovskite/silicon tandem solar cells are increasingly studied due to their potential for reaching record PCEs[11–14]. In these tandem stacks, the perovskite absorbers form the top cell and must, therefore, possess a wider bandgap with respect to the Si bottom cell. Ideally, E_g is in the range of ~1.67–1.75 eV[13,15], which is considerably higher than pure α-$FAPbI_3$ or $MAPbI_3$. One commonly applied strategy for increasing E_g of an MHP is to employ mixtures of halides by, for example, partially replacing I^- with Br^-[11,13,16].

Despite their high performance, PSCs suffer from poor stability arising from bulk and interfacial defects facilitating ion migration and leading to permeation of moisture and oxygen. Furthermore, in wide-bandgap mixed-halide perovskites, defects, in particular at the grain boundaries (GBs), can cause light-induced halide phase segregation[17–20] which leads to substantial efficiency losses under continuous operation. Consequently, there is an urgent need to find strategies for avoiding defect formation and passivating active defects, to improve the efficiency and stability of PSCs. To this end, there have been several reports of defect mitigation via compositional engineering[21–24], a multifunctional organic small molecule[25], and organic ammonium salts[26–28]. However, there is a lack of systematic studies into combined bulk and interface defect passivation as well as the prevention of light induced phase segregation in particular with wide-bandgap mixed-halide perovskites.

In this work, we scrutinize the molecular design of alkylammonium halide passivators for highly efficient and stable PSCs based on α-$FAPbI_3$ and $FA_{65}MA_{35}Pb(I_{65}Br_{35})_3$. We show that, unexpectedly, the hitherto unexplored compounds, *N*,*N*-dimethyloctylammonium iodide (DMOAI) and *N*,*N*-dimethyloctylammonium fluoride (DMOAF), significantly outperform the commonly used ammonium amphiphiles. By adding one of these compounds to the perovskite precursor solution and depositing the second onto the perovskite surface in a post-annealing step, we reached champion efficiencies of 24.9% and 21.2% for α-$FAPbI_3$- and $FA_{65}MA_{35}Pb(I_{65}Br_{35})_3$-based PSCs, respectively. This also greatly enhanced their operational stabilities with ~90% and ~80% of their original PCE retained after 1200 h and 250 h, respectively, of light soaking at full solar intensity under maximum power point tracking. Our in-depth experimental investigation revealed the suppression of unwanted photoinduced halide phase segregation in films of $FA_{65}MA_{35}Pb(I_{65}Br_{35})_3$, a Br-rich composition highly susceptible to this degradation pathway. Molecular dynamics and density functional theory studies were carried out to rationalize these observations by studying the binding of our additives to the surface and GBs of the perovskite, after 2D solid-state NMR had proven the atomic-scale proximity of the modulator and the perovskite.

Results:

Molecular Design, Device Performance, and Stability

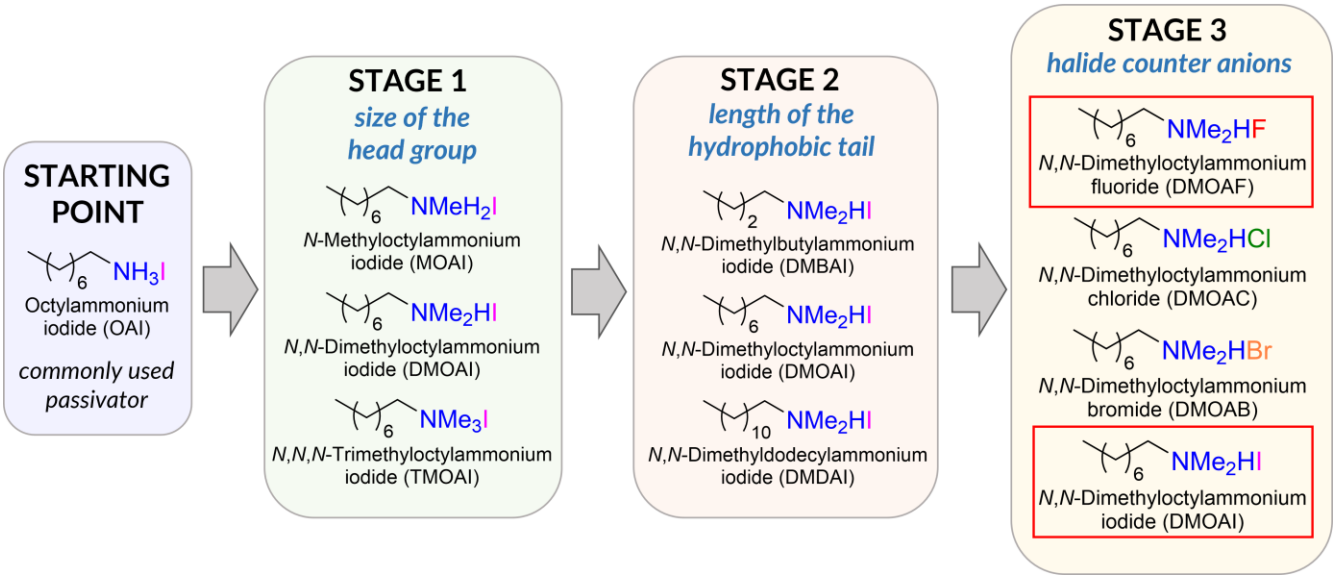

Figure 1. Systematic optimization of the organic ammonium halide passivators used in this study. Starting from the commonly used octylammonium iodide (first panel), first, the size of the head group was optimized by consecutively replacing all proton substituents of the ammonium functionality with methyl groups (second panel). This was followed by varying the length of the hydrophobic tail (third panel) and finally a screening of halide counter anions (fourth panel). The best performing compounds are highlighted in red.

We started our investigation from octylammonium iodide (OAI), an archetype material for perovskite passivation[29,30]. α-$FAPbI_3$ (E_g = 1.53 eV) was employed in an *n-i-p* device architecture of FTO/c-TiO_2/m-TiO_2/perovskite/spiro-OMeTAD/Au. The structure of the passivator was optimized in three stages (**Figure 1**), by systematically increasing the size of the ammonium head group by replacing H with Me, changing the length of the hydrophobic tail, and by varying the halide counter anion (Figure S1 and S2, Table S1–S6). Each compound shown in **Figure 1** was tested for bulk (B), surface (S), and combined bulk and surface treatment. While the former entailed mixing the passivator into the perovskite precursor solution, the latter refers to application of the passivator onto the surface of freshly prepared perovskite thin films. To our surprise, we consistently found tertiary dimethylammonium head groups to perform better than primary ammoniums. Combinations of the dimethyl ammonium head group with a C_8 tail and iodide (DMOAI) or fluoride (DMOAF) as the counter anion, were found to perform best in B and S treatment, respectively, achieving PCEs of 22.8% and 23.1%, compared to 21.2% for the Control device without treatment[23].

Combining these treatments (DMOAI(B)/DMOAF(S)) led to a PCE of 24.9% with a V_{oc} of 1.145 V, a FF higher than 84%, and negligible hysteresis, as shown in **Figure 2a**. The stabilized PCE obtained during MPP tracking in ambient air (15–25% relative humidity (RH)) under one sun illumination for 300 s was 20.3% and 24.5%, respectively, for the Control and DMOAI(B)/DMOAF(S) devices (inset in **Figure 2a**). **Figure 2b** shows the statistical distribution of the photovoltaic characteristics (J_{SC}, V_{OC}, FF, and PCE), showing improvements in all device parameters. The incident photon-to-current efficiency (IPCE) spectra and integrated current density (Figure S3a) of the DMOAI(B)/DMOAF(S)-based device are practically the same as those of the Control, which exhibits a bandgap of 1.53 eV (Figure S3b).

Expanding our findings to wider-bandgap $FA_{65}MA_{35}Pb(I_{65}Br_{35})_3$ (E_g = 1.71 V) we found our observations to be reversed with DMOAF and DMOAI giving the best results for bulk and surface treatment, respectively, achieving PCEs of 18.6% and 19.4% compared to 18.0% for the untreated Control (Figure S4, Table S7). Cooperative treatment with (DMOAF(B)/DMOAI(S)) raised the PCE sharply to 21.2%, with a remarkable V_{OC} of 1.30 V, which is among the highest reported for wide-bandgap MHP solar cells. Note also the negligible hysteresis in the *J–V* curve of the champion cell (**Figure 2c**). The inset in **Figure 2c** shows the stabilized PCE over a period of 300 s for the Control and DMOAF(B)/DMOAI(S) devices to be 15.8% and 20.7%, respectively. The statistical distribution of the photovoltaic characteristics (J_{SC}, V_{OC}, FF, and PCE) is summarized in **Figure 2d**, showing improvements in all device parameters. The IPCE spectra and integrated photocurrent density (Figure S5a) of the DMOAF(B)/DMOAI(S)-treated device show practically no change in the onset of the IPCE spectrum, and the inflection point as compared to the Control, yielding a bandgap of 1.71 eV (Figure S5b).

The different responses to B and S treatment of narrow and wide-bandgap systems were attributed, at least partially, to differences in binding strength of the various anions (Figure S6) and associated lattice mismatch (Supplementary Note 1).

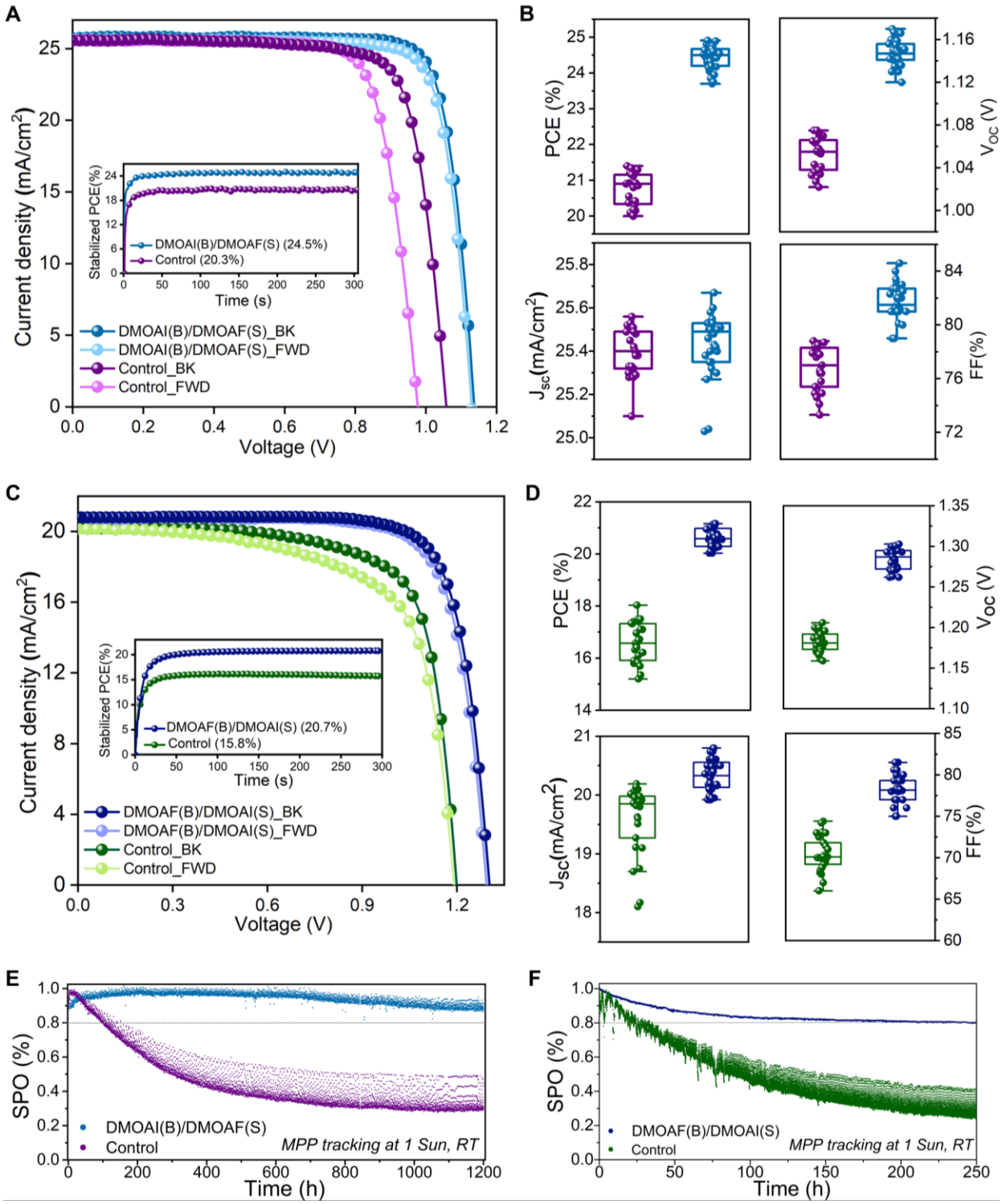

Figure 2. Optoelectronic properties and stability of narrow- and wide-bandgap devices. (**A**) *J–V* curves of the champion α-$FAPbI_3$-based Control and DMOAI(B)/DMOAF(S)-treated solar cells under reverse and forward scan. The inset shows the results of MPPT of the devices over the first 300 s in ambient air. (**B**) Summary of the photovoltaic metrics of α-$FAPbI_3$-based devices (purple: Control, blue: DMOAI(B)/DMOAF(S)). (**C**) *J–V* curves of the champion $FA_{65}MA_{35}Pb(I_{65}Br_{35})_3$-based Control and DMOAF(B)/DMOAI(S)-treated solar cells under reverse and forward scan. The inset shows the results of MPP tracking of the devices over the first 300 s in ambient air. (**D**) Summary of the photovoltaic metrics of $FA_{65}MA_{35}Pb(I_{65}Br_{35})_3$-based devices (green: Control, blue: DMOAF(B)/DMOAI(S)). (**E**+**F**) MPPT on unencapsulated α-$FAPbI_3$- (**E**) and $FA_{65}MA_{35}Pb(I_{65}Br_{35})_3$-based (**F**) solar cells using white LED light (100 $mWcm^{-2}$ in N_2, RT).

Shelf-life tests were conducted on Control, DMOAI(B)/DMOAF(S) α-$FAPbI_3$ and DMOAF(B)/DMOAI(S) $FA_{65}MA_{35}Pb(I_{65}Br_{35})_3$ devices by storing them at room temperature in the dark at 10% RH. In the case of the narrow bandgap perovskite, the Control and treated devices retained 86% and 97% of their initial performance, respectively, after 770 h (Figure S7a**),** whereas the wide bandgap perovskite devices retained 88% and 93%, respectively, after 480 h (Figure S7b). The operational stabilities of Control, DMOAI(B)/DMOAF(S) α-$FAPbI_3$ and DMOAF(B)/DMOAI(S) $FA_{65}MA_{35}Pb(I_{65}Br_{35})_3$ devices were studied by subjecting them to illumination at full solar intensity in a nitrogen atmosphere at room temperature with continuous maximum power point tracking (MPPT). The Control and treated α-$FAPbI_3$ devices retained ~25% and ~90%, respectively, of their initial performance after 1200 h, while the Control and treated $FA_{65}MA_{35}PB(I_{65}Br_{35})_3$ devices retained ~20% and ~80%, after 250 h illumination, respectively (**Figure 2e,f**). To evaluate the stability of our devices at elevated temperature and humidity, we repeated this test at 60 °C and 25% RH for periods of 240 h (narrow bandgap) and 145 h (wide bandgap), the Control devices maintained 39% and 20%, respectively, of their initial PCEs, whereas the treated devices maintained 78% and 81%, respectively (Figure S8a,b). Comparing SEM images of narrow bandgap perovskite films before and after aging at 65 °C and ~45% RH for 60 h revealed formation of PbI_2 and other white residuals during aging of untreated films whereas DMOAI(B)/DMOAF(S)-treated films remained unchanged (Figure S9a). In the case of wide bandgap films, both, Control and DMOAF(B)/DMOAI(S)-treated films, did not show changes in morphology following aging under these conditions (Figure S9b). In summary, this shows that treatment with our molecularly engineered dimethyl ammonium amphiphiles led to a substantial enhancement of the stability under different conditions with both perovskite compositions, outperforming other state-of-the-art systems (Table S8).

Molecular Interactions, Structure, Morphology, and Optoelectronic Properties

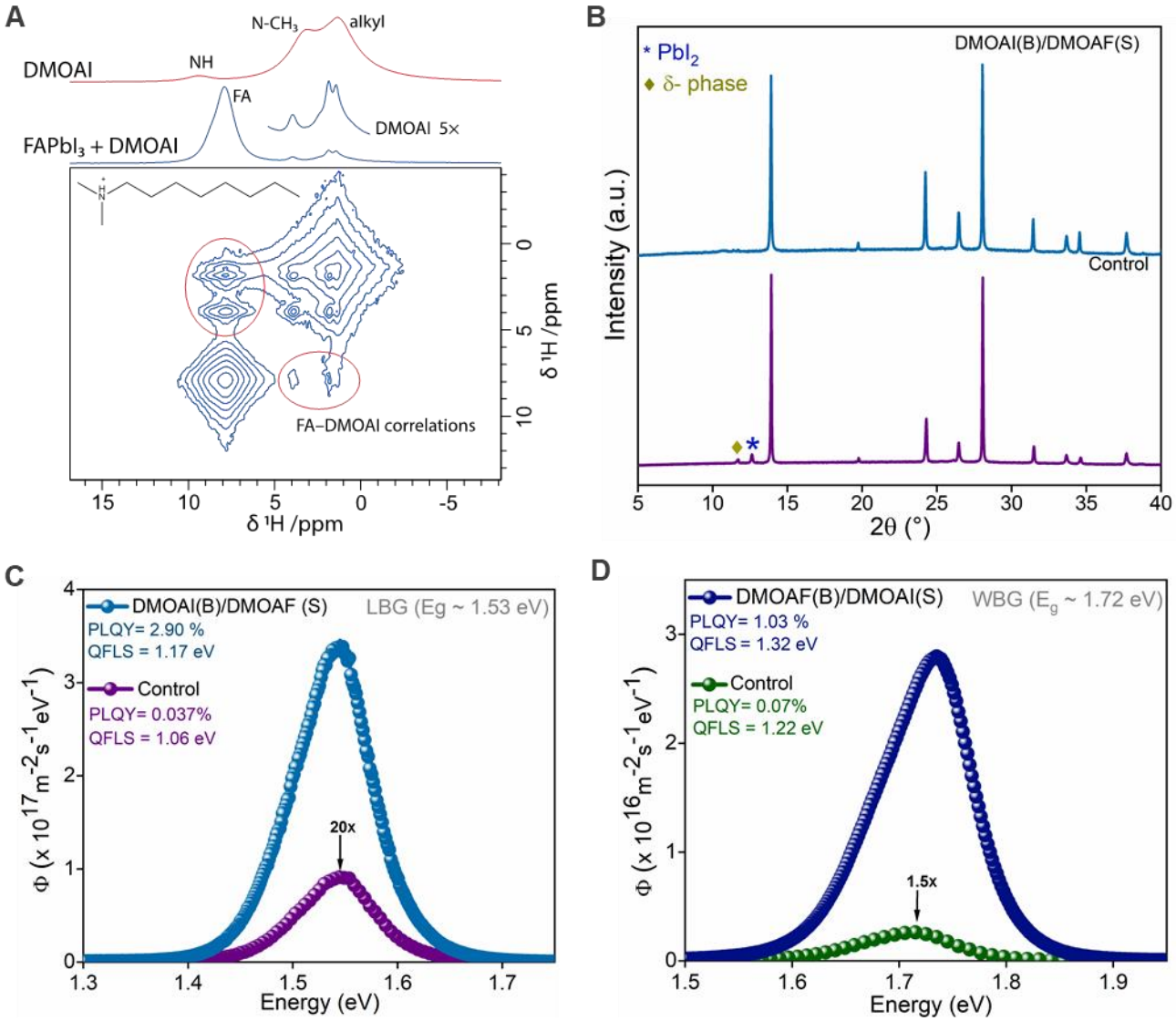

Figure 3. Characterization of perovskite thin films. (**A**) 2D ^{1}H–^{1}H spin diffusion NMR spectrum for a mechano-synthesized DMOAI(B) passivated α-$FAPbI_3$ perovskite. (**B**) X-ray diffractograms for samples of Control and DMOAI(B)/DMOAF(S)-treated α-$FAPbI_3$ perovskite films. (**C+D**) Absolute intensity PL spectra of Control and cooperatively treated devices based on α-$FAPbI_3$ (**C**) and $FA_{65}MA_{35}PB(I_{65}Br_{35})_3$ (**D**) measured at 1 sun steady-state illumination. The photoluminescence quantum yield (PLQY) and quasi-Fermi level splitting (QFLS) of each sample is reported. Note the asymmetry of the PL signals: The high energy shoulder is determined by the 300 K blackbody radiation whereas the low energy shoulder is determined by the Urbach energy (13 meV for α-$FAPbI_3$ and 15 meV for the $FA_{65}MA_{35}PB(I_{65}Br_{35})_3$ films) and by reabsorption (photon recycling).

To investigate the local molecular environment surrounding the ammonium group of the octyldimethylammonium amphiphile, solid-state NMR was performed on a sample of mechano-synthesized α-$FAPbI_3$ containing 1% DMOAI. In neat DMOAI, three broad resonances can be observed corresponding to the alkyl, methyl, and NH protons (**Figure 3a**, top). In the perovskite sample, the major methyl and alkyl signals from the additive can be observed but are sharper, indicating a lower proton density and, therefore, weaker dipolar coupling; two alkyl resonances can be distinguished, and the methyl signal is shifted to a higher frequency. These observations all show that the environment of the additive has changed substantially. In the ^1H–^1H spin diffusion spectrum (**Figure 3a**, bottom), cross-peaks are observed between the $DMOA^+$ and FA^+ resonances, proving that the perovskite and ammonium are in atomic-scale proximity, as has also been previously shown for other passivating agents[27,31–33]; this is consistent with adsorption at surfaces and grain boundaries.

X-ray diffraction (XRD) experiments showed a PbI_2 peak at 12.5° in Control, DMOAI(B), and DMOAF(S) α-$FAPbI_3$ samples, but not cooperatively treated DMOAI(B)/DMOAF(S) (**Figure 3b** and Figure S10). This indicates that PbI_2 had been fully consumed despite the perovskite precursor containing a 5% excess. Control and DMOAF(S) films also showed a peak at 11°, corresponding to the photo-inactive δ-phase. Formation of this phase was avoided in DMOAI(B) and DMOAI(B)/DMOAF(S) samples. Furthermore, we did not observe any low-dimensional secondary phases in any of our samples. The surface morphology in the SEM images (Figure S11) shows that the Control and DMOAI(B)/DMOAF(S) α-$FAPbI_3$ films are uniform and highly crystalline with similar compact textures and grain domain sizes of hundreds of nanometers.

Next, we investigated the optoelectronic properties of the Control and cooperatively treated perovskite films based on α-$FAPbI_3$ and $FA_{65}MA_{35}PB(I_{65}Br_{35})_3$. We measured absolute photoluminescence (PL) photon fluxes $\Phi_{PL}(E)$ of the Control and treated perovskite films with a hole transport layer (HTL) interface. Following established methods[34], the photoluminescence quantum yields (PLQY) were calculated as 2.9% and 0.037% for treated and untreated α-$FAPbI_3$ samples, respectively (**Figure 3c)**. For the wide-bandgap composition, they were determined as 1.0% and 0.07% for treated and untreated samples, respectively (**Figure 3d**). The increase in PLQY regardless of bandgap indicates a suppression of non-radiative recombination centers in the bulk and at the surface of the perovskite.

Charge carrier dynamics at the perovskite/HTL interface were studied using time-resolved PL (TRPL) spectroscopy (see Figure S12a,b). The fast decay at early times has been attributed to initial carrier trapping[35] and hole transfer[36], whereas the following slower decay is caused by non-radiative recombination and hole back-transfer[37]. We used low fluences to avoid radiative bimolecular or non-radiative Auger recombination being the dominant recombination mechanism[38]. At early times, the Control and DMOAI(B)/DMOAF(S)-treated α-$FAPbI_3$ films showed similar behavior (Figure S12a), but in the case of wide-bandgap films, we observed a faster initial decay in the DMOAF(B)/DMOAS(S)-treated sample compared to the Control, which indicates a faster hole transfer (Figure S12b)**.**

Suppression of Halide Phase Segregation in Wide-Bandgap Perovskite

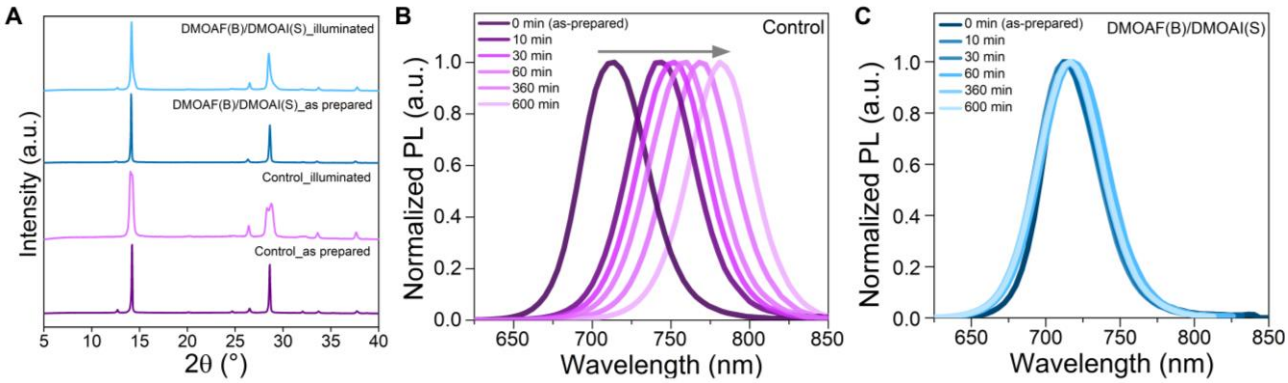

Figure 4. Effects of illumination on $FA_{65}MA_{35}Pb(I_{65}Br_{35})_3$ thin films (**A**) X-ray diffractograms for samples of Control and DMOAF(B)/DMOAS(S)-treated $FA_{65}MA_{35}PB(I_{65}Br_{35})_3$ perovskite films before and after illumination. (**B**+**C**) PL spectra of Control and DMOAF(B)/DMOAS(S)-treated $FA_{65}MA_{35}Pb(I_{65}Br_{35})_3$ films after different illumination times.

To study halide phase segregation in our wide-bandgap films, Control and DMOAF(B)/DMOAI(S)-treated $FA_{65}MA_{35}PB(I_{65}Br_{35})_3$ films were illuminated at an intensity of one sun for 10 h. The films were sealed in an argon environment, and continuous cooling was applied during illumination to avoid any effects related to moisture and temperature. XRD analysis (**Figure 4a**) showed clear halide phase segregation in the Control sample after illumination, as evidenced by the splitting of the reflections at ~14° and ~29°, caused by the small differences in the unit cell size of the bromide- and iodide-rich phases. In the treated sample, this halide segregation is substantially suppressed. Top-view SEM images of the aged Control and DMOAF(B)/DMOAI(S)-treated films revealed pinholes and clear signs of degradation for the aged Control sample, whereas the morphology of the aged DMOAF(B)/DMOAI(S)-treated film remained unchanged (Figure S13).

These results were confirmed by steady-state PL measurements showing a large, continuous red-shift during illumination for a Control film but only minimal changes for a film with DMOAF(B)/DMOAI(S) treatment (**Figure 4b,c**, Figure S14, S15). This is a remarkable observation due to the high Br^- content in the perovskite composition used. By repeating this experiment with films having only been treated either with DMOAF(B) or DMOAI(S) we demonstrated that this suppression of halide phase segregation is due to the bulk treatment with DMOAF (Figure S15).

Mechanistic Understanding – Molecular Dynamics and DFT

Computational studies were performed to understand how our additives interact with the surface of FA-based perovskites leading to the observed improvements in PCE and stability. Incorporation into the bulk material was ruled out based on the considerably larger size of our additives as compared to FA^+ (Figure S16). After optimizing the structures of OA^+, MOA^+, $DMOA^{+,}$ and $TMOA^+$ (Scheme 1) using density functional theory (DFT), their interaction with a model of the Pb-I terminated α-$FAPbI_3$ surface was investigated. In the resulting lowest-energy structures, OA^+ and $TMOA^+$ were in a perpendicular arrangement relative to the surface, whereas an almost parallel orientation was found for MOA^+ and $DMOA^+$ (**Figure 5a**, Figure S17). This tilting facilitates H-bond formation between their asymmetric head groups and the surface halide ions (**Figure 5a**, Figure S18**)** and leads to a more efficient coverage of the perovskite surface for the latter two compounds (38.7% and 40.7% for MOA^+ and $DMOA^+$ vs. 14.6% and 24.2% for OA^+ and $TMOA^+$; **Figure 5b**; Table S9), while at the same time impeding the formation of a 2D perovskite surface layer. Contrary to the fully symmetric head groups of OA^+ and $TMOA^+$, the asymmetric head groups of MOA^+ and $DMOA^+$ (containing two and one polar hydrogen atoms, respectively) are responsible for their distinct spatial orientation with respect to the perovskite surface (Figure 5a). For completeness, two further additives, *N*,*N*-dimethylbutylammonium ($DMBA^+$) and *N*,*N*-dimethyldodecylammonium ($DMDA^+$), were considered with the same head group but different tail lengths (four and twelve carbons, respectively). Simulation results showed that $DMOA^+$ had the highest proximity to the surface while having in-plane parallel to the surface orientational components commensurate to those of $DMDA^+$, thereby offering the best surface protection of the three (Figure S19). The higher coverage provides better protection from moisture as well as an increased stability against the detachment of halides and FA^+ ions from the surface. Studying

the interaction of our compounds with a surface FA^+ vacancy, their positively charged head groups were found to partially penetrate the negatively charged vacancy cavity establishing various N–H···I and C–H···I interactions (Figure S18). The decreasing number of strong N–H···I H-bonds going from OA^+ to MOA^+, $DMOA^+$ and finally $TMOA^+$ was compensated by an increasing number of short C–H···I contacts, keeping the differences between the overall binding strengths to within 0.2–0.4 eV (Table S10).

In the case of positively charged I^- vacancies, filling with I^- used as the alkylammonium counter anion and subsequent binding of the cations to surface I^- was considered as the likely mechanism of passivation. The binding strengths for the four different compounds show differences in the order of 0.1–0.5 eV with TMOAI having the strongest interaction (Table S11)**.** The orientation and tilting of the octyl chains were found to be the same as for the pristine surface.

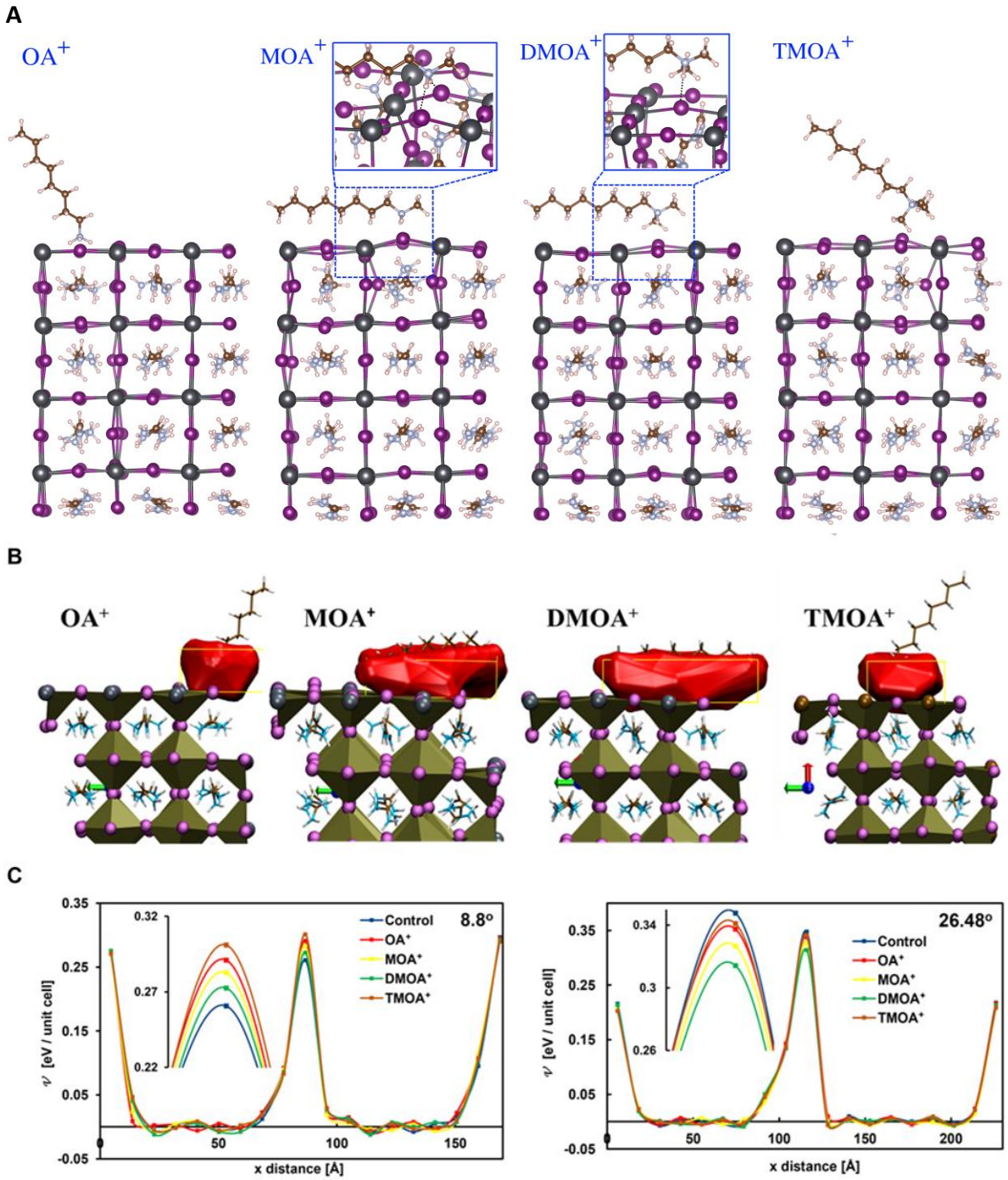

Figure 5. Interaction of passivators with the surface and grain boundaries of α-FAPbI$_3$. (**A**) Orientation of additive cations binding to a pristine Pb-I-terminated surface of α-FAPbI$_3$. The dotted lines indicate interactions of hydrogen atoms with iodides, leading to favorable binding. Hydrogen is shown in pink, carbon in brown, nitrogen in light grey, lead in dark grey, and iodine in purple. (**B**) Molecular representations of the covered surface area, shown in red, by each additive interacting with a pristine Pb-I-terminated α-FAPbI$_3$ surface. (**C**) Potential energy profiles from classical molecular dynamics simulations for two representative GBs (8.8° and 26.48°). For both GBs, five potential energy profiles are shown: for the pristine (Control) system and the four composite systems containing 5 molecules of OA$^+$, MOA$^+$, DMOA$^{+,}$ and TMOA$^+$, respectively. In both parts, the inset shows a magnification of the potential energy curves at the GB.

The effect of our additives on GBs was studied by calculating the time-averaged potential energy profiles normal to the GB plane using Molecular Dynamics (MD) simulations taking into consideration angles that have been observed to be dominant experimentally[39] (Figure S20, Table S12). In each case, GBs were found to constitute local potential energy maxima. The effect of the additives depends on the GB angle: GBs with angles of 13.42°, 18.92°, and 26.48° were stabilized in the presence of all four different cations (**Figure 5c** and Figure S21**),** whereas GBs with the more extreme angles of 8.8° and 48.89° were further destabilized (**Figure 5c** and Figure S20) due to the increased steric hindrance experienced by these compounds (Figure S16 and S22; Table S13) limiting their orientational degrees of freedom (Figure S23). For the first set, the effect was most pronounced with $DMOA^+$ while this cation caused the lowest energy increase in the second set. Together, these studies clearly demonstrate the superior passivation capacity of $DMOA^+$ due to its improved surface coverage, and an overall superior stabilization of GBs compared to the other studied head groups.

DFT and MD simulations also revealed a low halide vacancy formation energy of 0.16–0.22 eV in the untreated system accompanied by a lowering of the potential energy by 1.1 eV upon moving this defect from the bulk of the crystal grain to a GB. Adding any of the four studied cations to the system increased the formation energy (Table S14) and reduced the mobility of halide vacancies (Figure S24), with $DMOA^+$ and MOA^+ giving the best results. These effects are due to the stabilization of surface halide ions by hydrogen bond formation and steric shielding against halide loss at the perovskite surface. Since halide segregation has been demonstrated to be facilitated by halide vacancies promoting halide mobility[40–42], these observations likely explain the suppression of halide phase segregation in bulk treated $FA_{65}MA_{35}Pb(I_{65}Br_{35})_3$.

Conclusions:

In short, we have developed DMOAI and DMOAF, a set of ammonium halide amphiphiles, capable of synergistically boosting the PCE and stability of narrow as well as wide-bandgap PSCs based on α-$FAPbI_3$ and $FA_{65}MA_{35}Pb(I_{65}Br_{35})_3$, respectively. Critically, bulk treatment of the mixed-halide perovskite with DMOAF suppresses photoinduced halide phase segregation, which is a vital prerequisite for the development of

perovskite/silicon tandem cells. Our cooperative passivation method, therefore, addresses the most prominent current challenges in the field of PSCs. Detailed experimental and computational analyses provide a clear rational for our observations providing a framework for understanding perovskite-passivator interactions. In conclusion, we expect these results to help pave the way for large-scale practical applications of PSC technology.

Experimental Procedures

Synthesis and Characterization of Compounds

Reagents were purchased from Sigma Aldrich, Acros or TCI Europe and were used as received. Solvents were reagent grade and used without prior water removal unless otherwise indicated. Anhydrous solvents were obtained from Acros.

Solution-state ^{1}H, ^{19}F and ^{13}C NMR spectra were recorded on a Bruker Avance III 400 MHz NMR spectrometer at 298 K using a BBFO-Plus$_{Z}$ 5 mm probe. Multiplets in ^{1}H NMR spectra are designated as follows: s (singlet), d (doublet), t (triplet), q (quartet), p (pentet), s (sextet), m (multiplet), br (broad). NMR spectra were analyzed using MestReNova (version:14.1.2-25024) software.

High resolution mass spectrometry was either performed on an LTQ Orbitrap ELITE ETD (Thermo Fisher) equipped with the high-field Orbitrap™ mass analyzer, standard ESI (H-ESI II) and nanoESI (nanoSpray Flex Ion) sources, as well as the nanochip based ESI system Advion TriVera Nanomate®, or a Xevo® G2-S QTof (Waters) equipped with the StepWave™ ion optics, QuanTof™ technology, as well as the ESI-APCI source.

<u>General Procedure for Protonation of Free Amines</u>

The corresponding amine (2.00 mmol, 1.00 eq.) was dissolved in Et_2O (5.0 mL) before the desired hydrohalic acid (solution in H_2O; 2.00 mmol, 1.00 eq.) was added under vigorous stirring. The reaction was stirred for 30 min and the stir bar was removed. Solvents were removed *in vacuo* (rotary evaporator at 60 °C). Remaining water was removed by co-evaporation with anhydrous EtOH (2.0 mL, 3x), before adding anhydrous Et_2O (5.0 mL) to the remaining solid product. The mixture was sonicated to obtain a powdery product which was isolated by filtration

and washing with anhydrous Et_2O. This product was collected in a vial and dried overnight under reduced pressure before leaving it to further dry in a desiccator over P_2O_5 for one week.

Device Fabrication

Fluorine-doped tin oxide (FTO)-glass substrates (TCO glass, NSG 10, Nippon sheet glass, Japan) were etched and cleaned by ultrasonication in Hellmanex (2%, deionized water), rinsed thoroughly with de-ionized water and ethanol, and then treated in oxygen plasma for 30 min. Approximately, 25 to 30 nm of blocking layer (TiO_2) was sprayed on the cleaned FTO at 450 °C using a commercial titanium diisopropoxide bis(acetylacetonate) solution (75% in 2-propanol, Sigma-Aldrich) diluted in anhydrous ethanol (1:10 volume ratio). A 150 nm mesoporous TiO_2 layer (diluted paste (1:7 wt. ratio of Dyesol 30NRD:ethanol)) was applied by spin-coating at 5000 rpm for 15 s and then sintered at 450 °C for 30 min in dry air. The perovskite films were deposited using a single-step deposition method from the precursor solution which was prepared in an Argon atmosphere and contained 1.5 M of FAI and PbI_2 with an added 35–40 mol% of MACl in anhydrous dimethylformamide/dimethylsulphoxide (4:1 (volume ratio)) to achieve the desired composition: α-$FAPbI_3$ (5% PbI_2 excess). For bulk treatment, a 0.1 M stock solution of each additive in DMSO was prepared. These were subsequently added as excess to the perovskite precursor solutions to obtain different concentrations. For surface treatment, each additive was dissolved in IPA and after preparing the perovskite film the according sample was dynamically deposited. Device fabrication was carried out inside a dry air box, under controlled atmospheric conditions. Perovskite solution was spin-coated in a two-step program at 1000 followed by 5000 rpm. Subsequently, 270 µl of chlorobenzene were dropped on the spinning substrate. This was followed by annealing the films at 150 °C for 35–40 min. To complete device fabrication, 92 mg of 2,2',7,7'-tetrakis(*N*,*N*-di-*p*-methoxyphenylamine)-9,9-spirobifluorene (spiro-OMeTAD) were dissolved in 1 ml of chlorobenzene to be used as hole-transporting material (HTM). The HTM was spin-coated at 5000 rpm for 30 s and doped with bis(trifluoromethylsulfonyl)imide lithium salt (24 µl of a solution prepared by dissolving 520 mg LiTFSI in 1.0 ml of acetonitrile), and 40 µl of 4-tert-butylpyridine. Finally, a ~80 nm gold (Au) layer was applied via thermal evaporation.

The active device area was 0.25 cm^2 (0.5 cm x 0.5 cm). All measurements were conducted using a non-reflective metal mask with an aperture area of 0.158 cm^2 covering part of the active area of the devices and avoid capture of stray light. The mask area was determined using Micro-Vu Sol 161 precision measuring equipment.

Device Characterization

The current-voltage (*J*–*V*) characteristics of the perovskite devices were recorded at ambient temperature and air conditions without device preconditioning using a digital source meter (Keithley model 2400, USA). A 450 W xenon lamp (Oriel, USA) was used as the light source for photovoltaic (*J*–*V*) measurements (Figure S17). The spectral output of the lamp was filtered using a Schott K113 Tempax sunlight filter (Präzisions Glas & Optik GmbH, Germany) to reduce the mismatch between the simulated and actual solar spectrum to less than 2%. Before each measurement, the exact light intensity was determined using a calibrated Si reference diode equipped with an infrared cut-off filter (KG-3, Schott). The Si reference cell had been calibrated and certified by Newport Corporation PV Lab, Bozeman, MT, USA. The date of the calibration and certification was 30th August 2019. The photo-active area of 0.158 cm^2 was defined using a dark-colored metal mask. Voltage steps of 10 mV and a settling time of 100 ms was used. Scans were conducted in the range of 0–1.2 V and 0–1.4 V for low- and wide-bandgap PSCs, respectively. A polymer film stuck to the front glass was used as antireflection coating. For the box plots in Figure 2, at least 15 devices of each kind were tested.

Incident Photon-to-Current Efficiency (IPCE) Measurements

IPCE spectra were recorded under a constant white light bias of approximately 5 mW cm^{-2} supplied by an array of white light-emitting diodes. The excitation beam coming from a 300 W Xenon lamp (ILC Technology) was focused through a Gemini 180 double monochromator (Jobin Yvon Ltd) and chopped at approximately 2 Hz. The signal was recorded using a Model SR830 DSP lock-in amplifier (Stanford Research Systems).

Scanning Electron Microscopy (SEM)

SEM analysis was performed on a ZEISS Merlin HR-SEM.

Powder X-Ray Diffraction (XRD)

Powder X-ray diffractograms were recorded on a Bruker D8 Discover (Cu anode, λ = 1.54060 Å) in Bragg Brentano geometry, equipped with a Johansson $K\alpha_1$ monochromator and a Lynxeye XE detector. Lattice parameters were extracted from profile fitting using Topas 5.

Time-Resolved Photoluminescence (TRPL)

The photoluminescence lifetime was measured via time-correlated single-photon counting (TCSPC) using a LifeSpec II (Edinburgh Instruments) fluorescence spectrometer with a picosecond pulsed diode laser (EPL-510, Edinburgh Instruments) at 510 nm wavelength, 85 ps pulse width, and 4.5 nJ cm^{-2} fluence.

Solid-State NMR Measurements

Solid-state ^{1}H NMR spectra were recorded at room temperature and 11.7 T (500 MHz) with 1.3 mm outer-diameter rotors and a triple-resonance low-temperature magic angle spinning probe. ^{1}H–^{1}H spin diffusion spectra used 50 kHz magic angle spinning, rotor synchronised echo detection, pre-saturation, 125 kHz radiofrequency power, 140 steps of 100 μs in the indirect dimension, and a 1 s mixing time. A recycle delay of 1 s was used to partially suppress the signals originating on FA with a longer longitudinal relaxation constant (T_1 ~ 20 s), compared to the additive (T_1 ~ 1 s), due to the lower concentration of the latter; this results in an asymmetry of the cross peaks. The direct ^{1}H experiments used recycle delays of 3 s and 200 s for neat DMOAI and DMOAI-treated α-$FAPbI_3$, respectively.

Long-Term Light Soaking Test

Stability measurements were performed with a Biologic MPG2 potentiostat under a full AM 1.5 Sun-equivalent white LED lamp. The devices were measured with a maximum power point (MPP) tracking routine under continuous illumination at room temperature. The MPP was updated every 10 s by a standard perturb and observe method. Every minute a *J–V* curve was recorded in order to track the evolution of individual *J–V* parameters. The cells during the stability test were at room temperature. The sample holder in our stability set up contains a Peltier element which dissipates the heat and keeps the cells at room temperature. The temperature is kept constant and is monitored constantly with a built-in thermocouple.

Photoluminescence Quantum Yield (PLQY)

PLQY was determined following the procedure suggested by de Mello[43]. Samples were excited using a continuous-wave laser (OBIS LX, 660 nm) whose power was adjusted to match the photogeneration rate under one Sun illumination (0.324 mW, 0.786 mm effective beam FWHM). The signal was collected using an integrating sphere (Gigahertz Optik, UPB-150-ARTA) connected via a multimode, 400 µm diameter optical fiber (Thorlabs BFL44LS01) to a spectrometer (Andor, Kymera 193i). The system was spectrally calibrated using an irradiance calibration standard lamp (Gigahertz Optik, BN-LH250-V01).

Density Functional Theory (DFT)

DFT calculations were performed with the Quantum ESPRESSO package[44,45], using the PBEsol functional[46] with the correction of Grimme et al[44] to account for dispersion interactions. A plane-wave basis set in combination with pseudopotentials from the SSSP efficiency library was employed[42]. The basis set energy cutoff and reciprocal space grid were converged to 1 meV/atom for bulk $FAPbI_3$, yielding values of 62 Ry and a Gamma-centered grid of (6,6,6). To model the $FAPbI_3$ (100) surface, the periodic slab approach was used. Here, both the slab and vacuum size were converged with respect to the surface energy within 0.02 Jm^{-2} using Surfaxe[48], yielding a slab size of

four layers (21 Å) and a vacuum gap of 30 Å. To describe surface defects, the standard supercell approach was employed. In this framework, a 3×3×1 expansion of the slab was used to describe the dilute case and minimize spurious periodic image interactions. Given the large size of these systems, the Gamma point approximation was employed. All systems were geometrically optimized until the force on each atom was smaller than 10^{-5} a.u., and a dipole correction was employed to correct the spurious interaction between a polar slab and its periodic images. Initial structures with the additives were built manually based on the configurations obtained by previous classical molecular dynamics simulations. Finally, to calculate the binding affinities of the additives to the different perovskite surfaces, we computed the difference in energies between the bonded system (additive interacting with $FAPbI_3$) and its isolated parts (additive and $FAPbI_3$ separately).

Molecular Dynamics (MD) Simulations

Classical MD simulations with full atomistic resolution were utilized here to simulate the interactions of $FAPbI_3$ and four additives (OA^+, MOA^+, $DMOA^+$ and $TMOA^+$). Because grain boundaries (GBs) constitute relatively large two-dimensional crystallographic defects extending to several nm in length[39], classical MD simulations were deemed appropriate and were utilized here for this case.

The LAMMPS MD simulator[49] was used in the *NVT* and *NPT* statistical ensembles at T = 300 K and P = 1 atm (where applicable). The equations of motion were integrated using the Velocity-Verlet method, with a 1 fs time step. To maintain isothermal and isobaric conditions, the deterministic Nosé–Hoover thermostat and barostat[50], with constants of 0.1 and 1 ps, respectively, were utilized. Periodic boundary conditions were applied in all directions. Depending on the simulation type, each simulation ran for a total of 5 to 10 ns, the first 2 ns of which were excluded from the sampling process, taking place every 500 fs, to compute ensemble averages. To capture accurately the inter- and intra-molecular interactions in $FAPbI_3$, the classical force field, originally developed by Mattoni et al[51,52]. for methylammonium lead iodide ($MAPbI_3$), was recently tailored and refined to better match the interactions in $FAPbI_3$ resulting in the classical force field employed here[53]. The web-based LigParGen tool[54] was utilized to obtain all-atom OPLS interaction parameters for the alkylammonium cations considered here.

Size, Shape and Orientational Analysis of Additives

To gain insight into the average size, shape and orientation of the different additives with respect to $FAPbI_3$ surface during the MD, the chain gyration tensor **S** was employed. For a chain comprising *N* monomers, the chain gyration tensor is given by Eq. 1, where x_i, y_i and z_i are the position vector elements of monomer *i* and x_{cm}, y_{cm} and z_{cm} are those of the center of mass of each chain. Having calculated the time, sampled every 500 fs, and chain averaged **S** for every additive, various shape descriptors can be derived, such as the mean squared radius of gyration (first invariant of **S**), the relative anisotropy κ (second invariant) and the asphericity *b* measuring the deviation from the spherical symmetry. Here we chose to focus on the mean squared radius of gyration enclosing information on the size, shape and orientation of the additives with respect to the perovskite surface and GBs.

$$S = \frac{1}{N}\begin{pmatrix} \sum_{i=1}^{N}(x_i - x_{cm})^2 & \sum_{i=1}^{N}(x_i - x_{cm})(y_i - y_{cm}) & \sum_{i=1}^{N}(x_i - x_{cm})(z_i - z_{cm}) \\ \sum_{i=1}^{N}(x_i - x_{cm})(y_i - y_{cm}) & \sum_{i=1}^{N}(y_i - y_{cm})^2 & \sum_{i=1}^{N}(y_i - y_{cm})(z_i - z_{cm}) \\ \sum_{i=1}^{N}(x_i - x_{cm})(z_i - z_{cm}) & \sum_{i=1}^{N}(y_i - y_{cm})(z_i - z_{cm}) & \sum_{i=1}^{N}(z_i - z_{cm})^2 \end{pmatrix} \quad (1)$$

Polymeric oligomers in dilute solutions and melts usually have the shape of flattened (oblate) ellipsoids[55,56], however, when under spatial confinement, as in the case of GBs, elongated (prolate) ellipsoids are possible. The average size of a particular additive is measured by the mean squared radius of gyration

$$\left\langle R_g^2 \right\rangle = \frac{1}{N}\left\langle \sum_{i=1}^{N}(\mathbf{x}_i - \mathbf{x}_{cm})^2 \right\rangle \quad (2)$$

The explicit dimensions of the three chain semiaxes are described by the eigenvalues of the chain gyration tensor. The sum of the three average eigenvalues $\langle\lambda_i\rangle$, (i = x, y, z) equals the mean squared radius of gyration. The average dimension of each additive chain in each of its principal axes is given by the square root of the respective eigenvalue[57]. The three eigenvectors correspond to the orientation of each of the semiaxes defined by the particular chain conformation.

Grain Boundaries in $FAPbI_3$

GBs constitute two-dimensional (planar) crystallographic defects that are present in the majority of crystalline systems and are deemed regions of increased defect density and local disorder. This local disorder is supposed to be contributing to the reduced operational stability and efficiency of perovskite device. In the recent past, numerous studies employed several types of ammonium cations to passivate surface defects and GBs by reducing the charge carrier recombination losses[26,27,31,36]. To simulate the effect and passivation capacity of the four additives considered here (OA^+, MOA^+, $DMOA^+$ and $TMOA^+$) when added in the cavities of GBs in $FAPbI_3$, we constructed atomistic models of GBs exhibiting grain angles observed experimentally. Based on Rothmann et al.[39], $FAPbI_3$ grains approach each other at the following five dominant angles: 9.4°, 13.5°, 18.9°, 26.4° and 49.2°. The Aimsgb software[58] was utilized to build periodic GB structures with atomic resolution at angles that best approximated the experimentally observed ones. Figure S12 shows 2D floor plans of the five constructed $FAPbI_3$ model systems comprising grains coming together at 8.8°, 13.42°, 18.92°, 26.48° and 48.89°. In order to study the effect of the four additives (OA^+, MOA^+, $DMOA^+$ and $TMOA^+$) on the system's behavior, besides the "clean" pristine systems shown in Figure S12, we considered composite systems including each additive in the GB cavity. For studying the effect of concentration, the additives in the GBs were considered at two different concentrations, 5 and 10 molecules per model system, abbreviated as C_1 and C_2, respectively. Table S11 provides detailed information on the dimensions and number of atoms of the pristine and composite systems.

Accessible Volume and Surface Area Calculation

The estimation of the accessible volume within each GB was conducted with two different tools, both of which utilize the same principle, namely the insertion of a spherical probe atom with 1.0 Å radius within the GB cavity and the summation of each accessible incremental volume within a cutoff distance of 1.4 Å was used for the minimum distance between the outer surface of the probe sphere and the GB walls. The first tool was VolArea[59]; a plug-in of the widely used molecular visualization software Visual Molecular Dynamics (VMD)[60]. The second tool for the estimation of the accessible volume, was an in-house Python-based code utilizing the PyVista module[61], where the same specifications were used for the probe atom radius and cutoff distance. Both tools

delivered consistent results with relative differences lower than 2.5%. Finally, the estimation of the perovskite surface area covered by each one of the four additives considered here was conducted with the help of VolArea for a system comprising a pristine Pb-I terminated 3×3×3 $FAPbI_3$ slab and one single additive molecule.

Tracking Halide Vacancy Dynamics in $FAPbI_3$

To enrich our understanding of how the four additives influence halide vacancy mobility, we monitored the position over time of a halide vacancy originally introduced in the middle of one of the two grains. The position of the halide vacancy was tracked down by calculating every 25 fs the coordination number of all Pb ions. Undercoordinated Pb ions with a coordination number equal to five, instead of six, revealed the position of the mobile halide vacancy during a 1 ns long classical MD simulation in the *NVT* statistical ensemble. This computation was performed for all GB model systems shown in Figure S12. To enhance statistics, we considered and averaged over five independent, completely uncorrelated initial starting configurations of the halide vacancy. Next, the same calculation was repeated for systems now hosting five molecules of each additive in each one of the totally two different (due to periodic boundary conditions) GBs per system.

Data and Materials Availability:

All data are available in the main text or the supplementary materials.

Acknowledgments:

EAA gratefully acknowledges the support of King Abdulaziz City for Science and Technology (KACST), Saudi Arabia. AK., MAH. and GK acknowledge funding from the European Union's Horizon 2020 Research and Innovation program under the Marie Skłodowska-Curie Grant Agreement Nos. 843453, 101024144 and 101024237. LE acknowledges the Swiss National Science Foundation, Grant No. 200020_178860. UR acknowledges the Swiss National Science Foundation, Grant No. 200020_185092 and the NCCR-MUST for funding as well as computational resources from the Swiss National Computing Centre CSCS.

Author Contributions:

MG supervised the work. EAA conceived the idea of the work, designed and planned the experiments, fabricated most of the perovskite devices and did all the basic characterizations. EAA and LP discussed and designed the passivators. LP planned and carried out all the molecular synthesis with support from TC. AK, TPB, and GK contributed to the device fabrication. AK conducted the stability measurements. LP, and AK were involved in discussing the results throughout and at the end of the project. NL, MD, IML performed the DFT and classical MD calculations under the guidance of UR. MAH, AM, and LE carried out the ssNMR measurements and their analysis. OO recorded the PLQY and analyzed the PLQY data. FE analyzed the TRPL data. MG and SMZ guided the work and were involved in the interpretation of the obtained results. AH supervised AK. EAA, AK, and LP, wrote the first draft of the manuscript. All authors contributed to the preparation of the final manuscript.

Competing Interests:

EPFL has filed a PCT patent (PCT/IB2021/062185) related to the subject matter of this manuscript.

References:

1. Park, N.G., Grätzel, M., Miyasaka, T., Zhu, K., and Emery, K. (2016). Towards stable and commercially available perovskite solar cells. Nat. Energy *1*, 1–8.
2. Wojciechowski, K., Forgács, D., and Rivera, T. (2019). Industrial Opportunities and Challenges for Perovskite Photovoltaic Technology. Sol. RRL *3*, 1900144.
3. Li, D., Zhang, D., Lim, K.-S., Hu, Y., Rong, Y., Mei, A., Park, N.-G., and Han, H. (2021). A Review on Scaling Up Perovskite Solar Cells. Adv. Funct. Mater. *31*, 2008621.
4. Roy, P., Kumar Sinha, N., Tiwari, S., and Khare, A. (2020). A review on perovskite solar cells: Evolution of architecture, fabrication techniques, commercialization issues and status. Sol. Energy *198*, 665–688.
5. Kojima, A., Teshima, K., Shirai, Y., and Miyasaka, T. (2009). Organometal halide perovskites as visible-light sensitizers for photovoltaic cells. J. Am. Chem. Soc. *131*, 6050–6051.

6. Mannino, G., Deretzis, I., Smecca, E., La Magna, A., Alberti, A., Ceratti, D., and Cahen, D. (2020). Temperature-Dependent Optical Band Gap in CsPbBr3, MAPbBr3, and FAPbBr3 Single Crystals. J. Phys. Chem. Lett. *11*, 2490–2496.

7. Zhang, Y., Kim, S.G., Lee, D.K., and Park, N.G. (2018). CH3NH3PbI3 and HC(NH2)2PbI3 Powders Synthesized from Low-Grade PbI2: Single Precursor for High-Efficiency Perovskite Solar Cells. ChemSusChem *11*, 1813–1823.

8. Gu, L., Zhang, D., Kam, M., Zhang, Q., Poddar, S., Fu, Y., Mo, X., and Fan, Z. (2018). Significantly improved black phase stability of FAPbI3 nanowires via spatially confined vapor phase growth in nanoporous templates. Nanoscale *10*, 15164–15172.

9. https://www.nrel.gov/pv/cell-efficiency.html, accessed on 21.06.2022.

10. Shockley, W., and Queisser, H.J. (1961). Detailed balance limit of efficiency of p-n junction solar cells. J. Appl. Phys. *32*, 510–519.

11. Kamaraki, C., Klug, M.T., Green, T., Miranda Perez, L., and Case, C. (2021). Perovskite/silicon tandem photovoltaics: Technological disruption without business disruption. Appl. Phys. Lett. *119*, 70501.

12. De Bastiani, M., Van Kerschaver, E., Jeangros, Q., Ur Rehman, A., Aydin, E., Isikgor, F.H., Mirabelli, A.J., Babics, M., Liu, J., Zhumagali, S., et al. (2021). Toward Stable Monolithic Perovskite/Silicon Tandem Photovoltaics: A Six-Month Outdoor Performance Study in a Hot and Humid Climate. ACS Energy Lett. *6*, 2944–2951.

13. Wang, Z., Song, Z., Yan, Y., Liu, S. (Frank), and Yang, D. (2019). Perovskite—a Perfect Top Cell for Tandem Devices to Break the S–Q Limit. Adv. Sci. *6*, 1801704.

14. Liu, J., Aydin, E., Yin, J., De Bastiani, M., Isikgor, F.H., Rehman, A.U., Yengel, E., Ugur, E., Harrison, G.T., Wang, M., et al. (2021). 28.2%-efficient, outdoor-stable perovskite/silicon tandem solar cell. Joule *5*, 3169–3186.

15. Wang, R., Huang, T., Xue, J., Tong, J., Zhu, K., and Yang, Y. (2021). Prospects for metal halide perovskite-based tandem solar cells. Nat. Photonics *15*, 411–425.

16. Zhou, Y., Jia, Y.-H., Fang, H.-H., Loi, M.A., Xie, F.-Y., Gong, L., Qin, M.-C., Lu, X.-H., Wong, C.-P., and Zhao, N. (2018). Composition-Tuned Wide Bandgap Perovskites: From Grain Engineering to Stability and Performance Improvement. Adv. Funct. Mater. *28*, 1803130.

17. Zhao, Y., Miao, P., Elia, J., Hu, H., Wang, X., Heumueller, T., Hou, Y., Matt, G.J., Osvet, A., Chen, Y.-T., et al. (2020). Strain-activated light-induced halide segregation in mixed-halide perovskite solids. Nat.

Commun. *11*, 6328.

18. Phung, N., Al-Ashouri, A., Meloni, S., Mattoni, A., Albrecht, S., Unger, E.L., Merdasa, A., and Abate, A. (2020). The Role of Grain Boundaries on Ionic Defect Migration in Metal Halide Perovskites. Adv. Energy Mater. *10*, 1903735.

19. Motti, S.G., Patel, J.B., Oliver, R.D.J., Snaith, H.J., Johnston, M.B., and Herz, L.M. (2021). Phase segregation in mixed-halide perovskites affects charge-carrier dynamics while preserving mobility. Nat. Commun. *12*, 6955.

20. Kim, G.Y., Senocrate, A., Wang, Y.-R., Moia, D., and Maier, J. (2021). Photo-Effect on Ion Transport in Mixed Cation and Halide Perovskites and Implications for Photo-Demixing. Angew. Chem. Int. Ed. *60*, 820–826.

21. Belisle, R.A., Bush, K.A., Bertoluzzi, L., Gold-Parker, A., Toney, M.F., and McGehee, M.D. (2018). Impact of Surfaces on Photoinduced Halide Segregation in Mixed-Halide Perovskites. ACS Energy Lett. *3*, 2694–2700.

22. Alharbi, E.A., Baumeler, T.P., Krishna, A., Alyamani, A.Y., Eickemeyer, F.T., Ouellette, O., Pan, L., Alghamdi, F.S., Wang, Z., Alotaibi, M.H., et al. (2021). Formation of High-Performance Multi-Cation Halide Perovskites Photovoltaics by δ-CsPbI3/δ-RbPbI3 Seed-Assisted Heterogeneous Nucleation. Adv. Energy Mater. *11*, 2003785.

23. Alharbi, E.A., Krishna, A., Baumeler, T.P., Dankl, M., Fish, G.C., Eickemeyer, F., Ouellette, O., Ahlawat, P., Škorjanc, V., John, E., et al. (2021). Methylammonium Triiodide for Defect Engineering of High-Efficiency Perovskite Solar Cells. ACS Energy Lett. *6*, 3650–3660.

24. Saliba, M., Matsui, T., Seo, J.Y., Domanski, K., Correa-Baena, J.P., Nazeeruddin, M.K., Zakeeruddin, S.M., Tress, W., Abate, A., Hagfeldt, A., et al. (2016). Cesium-containing triple cation perovskite solar cells: improved stability, reproducibility and high efficiency. Energy Environ. Sci. *9*, 1989–1997.

25. Krishna, A., Zhang, H., Zhou, Z., Gallet, T., Dankl, M., Ouellette, O., Eickemeyer, F.T., Fu, F., Sanchez, S., Mensi, M., et al. (2021). Nanoscale interfacial engineering enables highly stable and efficient perovskite photovoltaics. Energy Environ. Sci. *14*, 5552–5562.

26. Zhu, H., Liu, Y., Eickemeyer, F.T., Pan, L., Ren, D., Ruiz-Preciado, M.A., Carlsen, B., Yang, B., Dong, X., Wang, Z., et al. (2020). Tailored Amphiphilic Molecular Mitigators for Stable Perovskite Solar Cells with 23.5% Efficiency. Adv. Mater. *32*, 1907757.

27. Alharbi, E.A., Alyamani, A.Y., Kubicki, D.J., Uhl, A.R., Walder, B.J., Alanazi, A.Q., Luo, J., Burgos-Caminal, A., Albadri, A., Albrithen, H., et al. (2019). Atomic-level passivation mechanism of ammonium

salts enabling highly efficient perovskite solar cells. Nat. Commun. *10*, 1–9.

28. Akin, S., Dong, B., Pfeifer, L., Liu, Y., Graetzel, M., and Hagfeldt, A. (2021). Organic Ammonium Halide Modulators as Effective Strategy for Enhanced Perovskite Photovoltaic Performance. Adv. Sci. *8*, 2004593.

29. Jeong, J., Kim, M., Seo, J., Lu, H., Ahlawat, P., Mishra, A., Yang, Y., Hope, M.A., Eickemeyer, F.T., Kim, M., et al. (2021). Pseudo-halide anion engineering for α-FAPbI3 perovskite solar cells. Nature *592*, 381–385.

30. Kim, H., Lee, S., Lee, D.Y., Paik, M.J., Na, H., Lee, J., and Seok, S. Il (2019). Optimal Interfacial Engineering with Different Length of Alkylammonium Halide for Efficient and Stable Perovskite Solar Cells. Adv. Energy Mater. *9*, 1902740.

31. Krishna, A., Akhavan Kazemi, M.A., Sliwa, M., Reddy, G.N.M., Delevoye, L., Lafon, O., Felten, A., Do, M.T., Gottis, S., and Sauvage, F. (2020). Defect Passivation via the Incorporation of Tetrapropylammonium Cation Leading to Stability Enhancement in Lead Halide Perovskite. Adv. Funct. Mater. *30*, 1909737.

32. Zhu, H., Pan, L., Eickemeyer, F.T., Hope, M.A., Ouellette, O., Qasem, A., Alanazi, M., Gao, J., Baumeler, T.P., Li, X., et al. (2022). Efficient and Stable Large Bandgap MAPbBr3 Perovskite Solar Cell Attaining an Open Circuit Voltage of 1.65 V. ACS Energy Lett. *17*, 1112–1119.

33. Kubicki, D.J., Stranks, S.D., Grey, C.P., and Emsley, L. (2021). NMR spectroscopy probes microstructure, dynamics and doping of metal halide perovskites. Nat. Rev. Chem. *5*, 624–645.

34. de Mello, J.C., Wittmann, H.F., and Friend, R.H. (1997). An improved experimental determination of external photoluminescence quantum efficiency. Adv. Mater. *9*, 230–232.

35. Trimpl, M.J., Wright, A.D., Schutt, K., Buizza, L.R. V, Wang, Z., Johnston, M.B., Snaith, H.J., Müller-Buschbaum, P., and Herz, L.M. (2020). Charge-Carrier Trapping and Radiative Recombination in Metal Halide Perovskite Semiconductors. Adv. Funct. Mater. *30*, 2004312.

36. Haddad, J., Krogmeier, B., Klingebiel, B., Krückemeier, L., Melhem, S., Liu, Z., Hüpkes, J., Mathur, S., and Kirchartz, T. (2020). Analyzing Interface Recombination in Lead-Halide Perovskite Solar Cells with Organic and Inorganic Hole-Transport Layers. Adv. Mater. Interfaces *7*, 2000366.

37. Krückemeier, L., Krogmeier, B., Liu, Z., Rau, U., and Kirchartz, T. (2021). Understanding Transient Photoluminescence in Halide Perovskite Layer Stacks and Solar Cells. Adv. Energy Mater. *11*, 2003489.

38. Kirchartz, T., Márquez, J.A., Stolterfoht, M., and Unold, T. (2020). Photoluminescence-Based

Characterization of Halide Perovskites for Photovoltaics. Adv. Energy Mater. *10*, 1904134.

39. Uller Rothmann, M., Kim, J.S., Borchert, J., Lohmann, K.B., O'Leary, C.M., Sheader, A.A., Clark, L., Snaith, H.J., Johnston, M.B., Nellist, P.D., et al. (2020). Atomic-scale microstructure of metal halide perovskite. Science *370*, eabb5940.

40. Yuan, Y., Chae, J., Shao, Y., Wang, Q., Xiao, Z., Centrone, A., and Huang, J. (2015). Photovoltaic Switching Mechanism in Lateral Structure Hybrid Perovskite Solar Cells. Adv. Energy Mater. *5*, 1500615.

41. Azpiroz, J.M., Mosconi, E., Bisquert, J., and De Angelis, F. (2015). Defect migration in methylammonium lead iodide and its role in perovskite solar cell operation. Energy Environ. Sci. *8*, 2118–2127.

42. Yoon, S.J., Kuno, M., and Kamat, P. V. (2017). Shift Happens. How Halide Ion Defects Influence Photoinduced Segregation in Mixed Halide Perovskites. ACS Energy Lett. *2*, 1507–1514.

43. De Mello, J.C., Wittmann, H.F., and Friend, R.H. (1997). An improved experimental determination of external photoluminescence quantum efficiency. Adv. Mater. *9*, 230–232.

44. Giannozzi, P., Baseggio, O., Bonfà, P., Brunato, D., Car, R., Carnimeo, I., Cavazzoni, C., De Gironcoli, S., Delugas, P., Ferrari Ruffino, F., et al. (2020). Quantum ESPRESSO toward the exascale. J. Chem. Phys. *152*, 154105.

45. Giannozzi, P., Baroni, S., Bonini, N., Calandra, M., Car, R., Cavazzoni, C., Ceresoli, D., Chiarotti, G.L., Cococcioni, M., Dabo, I., et al. (2009). QUANTUM ESPRESSO: A modular and open-source software project for quantum simulations of materials. J. Phys. Condens. Matter *21*, 395502.

46. Perdew, J.P., Ruzsinszky, A., Csonka, G.I., Vydrov, O.A., Scuseria, G.E., Constantin, L.A., Zhou, X., and Burke, K. (2008). Restoring the Density-Gradient Expansion for Exchange in Solids and Surfaces. Phys. Rev. Lett. *100*, 136406.

47. Prandini, G., Marrazzo, A., Castelli, I.E., Mounet, N., and Marzari, N. (2018). Precision and efficiency in solid-state pseudopotential calculations. npj Comput. Mater. *4*, 72.

48. Brlec, K., Davies, D., and Scanlon, D. (2021). Surfaxe: Systematic surface calculations. J. Open Source Softw. *6*, 3171.

49. Plimpton, S. (1995). Fast parallel algorithms for short-range molecular dynamics. J. Comput. Phys. *117*, 1–19.

50. Swope, W.C., Andersen, H.C., Berens, P.H., and Wilson, K.R. (1982). A computer simulation method for

the calculation of equilibrium constants for the formation of physical clusters of molecules: Application to small water clusters. J. Chem. Phys. *76*, 637–649.

51. Mattoni, A., Filippetti, A., and Caddeo, C. (2016). Modeling hybrid perovskites by molecular dynamics. J. Phys. Condens. Matter *29*, 43001.

52. Mattoni, A., Filippetti, A., Saba, M.I., and Delugas, P. (2015). Methylammonium Rotational Dynamics in Lead Halide Perovskite by Classical Molecular Dynamics: The Role of Temperature. J. Phys. Chem. C *119*, 17421–17428.

53. Paramvir, A., Alexander, H., A., A.E., Haizhou, L., Amita, U., Haiyang, N., Michele, I., Mohammed, Z.S., Ibrahim, D.M., Frank, S., et al. (2022). A combined molecular dynamics and experimental study of two-step process enabling low-temperature formation of phase-pure α-FAPbI3. Sci. Adv. *7*, eabe3326.

54. Dodda, L.S., De Vaca, I.C., Tirado-Rives, J., and Jorgensen, W.L. (2017). LigParGen web server: An automatic OPLS-AA parameter generator for organic ligands. Nucleic Acids Res. *45*, W331–W336.

55. Theodorou, D.N., and Suter, U.W. (1985). Shape of unperturbed linear polymers: polypropylene. Macromolecules *18*, 1206–1214.

56. Wolf, R.M., and Suter, U.W. (1984). Conformational characteristics of poly(vinyl alcohol). Macromolecules *17*, 669–677.

57. Doxastakis, M., Chen, Y.-L., Guzmán, O., and de Pablo, J.J. (2004). Polymer–particle mixtures: Depletion and packing effects. J. Chem. Phys. *120*, 9335–9342.

58. Cheng, J., Luo, J., and Yang, K. (2018). Aimsgb: An algorithm and open-source python library to generate periodic grain boundary structures. Comput. Mater. Sci. *155*, 92–103.

59. Ribeiro, J. V, Tamames, J.A.C., Cerqueira, N.M.F.S.A., Fernandes, P.A., and Ramos, M.J. (2013). Volarea – A Bioinformatics Tool to Calculate the Surface Area and the Volume of Molecular Systems. Chem. Biol. Drug Des. *82*, 743–755.

60. Humphrey, W., Dalke, A., and Schulten, K. (1996). VMD: Visual molecular dynamics. J. Mol. Graph. *14*, 33–38.

61. Sullivan, C., and Kaszynski, A. (2019). PyVista: 3D plotting and mesh analysis through a streamlined interface for the Visualization Toolkit (VTK). J. Open Source Softw. *4*, 1450.